

## Article

# Microstructure and Mechanical Properties of Al-Cu-Mg Alloy Fabricated by Double-Wire CMT Arc Additive Manufacturing

Siyue Fan <sup>1</sup>, Xinpeng Guo <sup>2</sup>, Yan Tang <sup>1</sup> and Xuming Guo <sup>1,\*</sup>

<sup>1</sup> School of Materials Science and Engineering, Shenyang Aerospace University, Shenyang 110136, China; fansiyue123@sina.com (S.F.); tangyan361@163.com (Y.T.)

<sup>2</sup> School of Mechanical, Materials, and Mechatronics Engineering, Faculty of Engineering and Information Sciences, University of Wollongong, Northfield Ave, Wollongong, NSW 2500, Australia; xg919@uowmail.edu.au

\* Correspondence: guoxuming@sau.edu.cn

**Abstract:** The high cracking sensitivity of Al-Cu-Mg alloy limits its application in wire + arc additive manufacturing (WAAM). In this paper, a double-wire cold metal transfer (CMT) arc additive manufacturing system was applied. ER2319 and ER5183 wires were selected as feedstocks and a new type of high-strength, crack-free Al-Cu-Mg alloy was manufactured. T6 (solution and artificial aging) heat treatment was conducted to further improve the mechanical properties. The microstructure, the second phase, distribution of main alloy elements and fracture morphology of Al-Cu-Mg alloys in both as-deposited and T6 heat-treated conditions were analyzed by optical micrographs (OM), X-ray diffraction (XRD), and scanning electron microscopy (SEM), respectively. The micro-hardness and tensile properties of WAAM Al-Cu-Mg alloy in both as-deposited and T6 heat-treated conditions were tested. The results demonstrated that the microstructure of the as-deposited Al-Cu-Mg alloy was composed of short rod-shaped columnar grains, equiaxed grains in the inter-layer region, and coarsened equiaxed grains in the inner-layer region; most of the second phases were continuously distributed along the grain boundaries. After the T6 heat treatment,  $\alpha(\text{Al})$  grains became coarsened, most of second phases were dissolved, and the Cu and Mg elements were distributed homogeneously in the aluminum matrix. The micro-hardness and strength were significantly improved but the elongation was reduced.

**Keywords:** double-wire CMT arc additive manufacturing; Al-Cu-Mg alloy; heat treatment; microstructure; mechanical property



**Citation:** Fan, S.; Guo, X.; Tang, Y.; Guo, X. Microstructure and Mechanical Properties of Al-Cu-Mg Alloy Fabricated by Double-Wire CMT Arc Additive Manufacturing. *Metals* **2022**, *12*, 416. <https://doi.org/10.3390/met12030416>

Academic Editor: Marco Mandolini

Received: 24 December 2021

Accepted: 25 February 2022

Published: 26 February 2022

**Publisher's Note:** MDPI stays neutral with regard to jurisdictional claims in published maps and institutional affiliations.



**Copyright:** © 2022 by the authors. Licensee MDPI, Basel, Switzerland. This article is an open access article distributed under the terms and conditions of the Creative Commons Attribution (CC BY) license (<https://creativecommons.org/licenses/by/4.0/>).

## 1. Introduction

Al-Cu alloys are widely applied in aerospace industries due to their high specific strength and excellent processing properties [1,2]. However, traditional manufacturing processes, such as casting or forging, not only have long processing cycles, but also have low material utilization rates to manufacture Al-Cu alloy components. Wire + arc additive manufacturing (WAAM), a rapid near net-shape method, adopts arc as the heat source, melting and depositing the filler wires along the designed path to manufacture large structural components, which has attracted attention of many researchers [3–5]. WAAM is extremely suitable for rapidly manufacturing medium and large metallic structures with advantages in high depositing efficiency, low cost of equipment, and flexibility of materials and design [6–8].

Al-Cu-Mg alloys are the highest strength aluminum alloys among Al2000 series aluminum alloys. However, when the Mg element was added in Al-Cu alloy, the brittle temperature range would be increased because the eutectic S phases ( $\text{Al}_2\text{CuMg}$ ) with low melting point were precipitated along the grain boundaries and the solubility of Cu in Al-Cu alloy was reduced [9,10]. Thus, the hot crack sensitivity of the alloy is increased. Fixter et al. reported that it is feasible to manufacture 2024-Al alloy by WAAM. However, its high

sensitivity to hot cracking must be considered [11]. Zhang et al. fabricated 2024-Al alloy thin wall structure by single-wire arc additive manufacturing, and apparent solidification cracks were found in the alloy [12]. Gu et al. manufactured 2024-Al alloy thin wall structure by single-wire cold metal transfer (CMT) arc additive manufacturing and studied the microstructure, defects, and mechanical properties. The ultimate tensile strength (UTS) and yield strength (YS) of alloy were 485 MPa and 399 MPa, respectively, in the horizontal direction after the T6 heat treatment. However, solidification cracks were the main reason for the brittle fracture, and the elongation was reduced in the vertical direction [13].

In summary, it is challenging to use existing Al-Cu-Mg alloy wire to produce high-strength, crack-free Al-Cu-Mg alloy by WAAM. Thus, a new Al-Cu-Mg wire suitable for WAAM should be developed. However, the developing of new aluminum alloy wire needs to go through the processes of smelting, extrusion, rolling, annealing, and drawing. Therefore, the production cycle is very long. In addition, in order to determine the best alloy composition, it is necessary to manufacture a large number of wires for verification, which is very expensive as well.

The research demonstrates that double-wire arc additive manufacturing provides a new method to manufacture Al-Cu-Mg alloy. Qi et al. selected ER2319 and ER5087 wires as feedstocks by using double-wire gas tungsten arc welding (GTAW) to produce Al-3.6Cu-2.2Mg, Al-4.0Cu-1.8Mg, and Al4.4Cu-1.5Mg alloys through adjusting the wire feed speeds (WFS). The horizontal UTS of these Al-Cu-Mg alloys had little difference and all exceeded 280 MPa. However, the YS of these Al-Cu-Mg alloys increased from 156 MPa to 177 MPa with higher Cu and lower Mg content, and the elongation decreased from 8.2% to 6% [14]. Gu et al. used double-wire gas metal arc welding (GMAW) to fabricate a series of Al-Cu-Mg alloys by adjusting the types of wires and the WFS. The effect of alloy composition on the cracking tendency was studied, and the results demonstrated that the Al-(4.2–6.3) Cu-(0.8–1.5) Mg alloys had a low cracking tendency [15].

The CMT process is considered as the most suitable method for WAAM applications due to its advantages of low heat input, stable wire feeding, less spatter, and good surface formation [16,17]. However, double-wire CMT additive manufacturing for manufacturing Al-Cu-Mg alloys was not reported yet. In this paper, a double-wire CMT additive manufacturing system was applied to manufacture a new high-strength, crack-free Al-Cu-Mg alloy by using ER2319 and ER5183 wires. The microstructure and mechanical properties of WAAM Al-Cu-Mg alloys in both as-deposited and T6 heat-treated conditions were studied.

## 2. Materials and Methods

The double-wire CMT additive manufacturing system is shown in Figure 1a. The system consists of two Fronius CMT advanced welding power sources, two wire feeders, a robotic arm (KUKA), and a dual-wire integrated welding gun. Two wires were fed simultaneously into the same molten pool in CMT mode during welding, as shown in Figure 1b.

2219-Al alloy plate (dimension in 200 mm × 50 mm × 15 mm) was selected as substrate, and ER2319 and ER5183 wires (diameter in 1.2 mm) were used as feedstocks. Their nominal chemical compositions are listed in Table 1.

The Al-Cu-Mg alloy component with 130 mm in length and 80 mm in height was manufactured, as shown in Figure 1c. The following parameters were set as constants for each layer: travel speed was 0.6 m/min; inter-layer cooling was 30 s; the flow rate of pure Ar (99.99%) was 25 L/min; and the distance between the contact tip and workpiece was set as 15 mm. For ER2319 wire, the WFS was 9 m/min, current was 160 A, and voltage was 15 V. For ER5183 wire, the WFS was 4.5 m/min, current was 80 A, and voltage was 8.7 V. The inductively coupled plasma optical emission spectrometer (ICP-OES) (Optima 8300 PerkinElmer, Waltham, MA, USA) was used to detect the Cu and Mg content of the WAAM Al-Cu-Mg alloy. The results demonstrated that the alloy contained 4.7% Cu and 2% Mg. Therefore, it can be referred to as the WAAM Al-4.7Cu-2Mg alloy in this article.

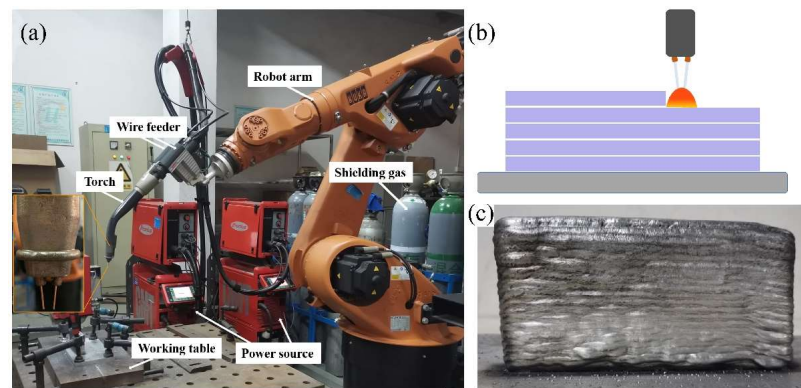


**Figure 1.** (a) Double-wire CMT additive manufacturing system, (b) schematic diagram of double wires depositing process, and (c) WAAM Al-Cu-Mg alloy wall.

**Table 1.** Nominal composition (wt.%) of ER2319, ER5183, and 2219 substrate.

Alloys	Cu	Mg	Mn	Fe	Si	Zr	Ti	Al
ER2319 wire	6.3	-	0.4	0.3	0.2	0.15	0.15	Bal.
ER5183 wire	-	5.0	0.6	0.2	0.2	-	0.1	Bal.
2219 substrate	6.3	-	0.2	0.3	0.2	0.15	0.1	Bal.

T6 heat treatment includes solution treatment and artificial aging treatment. The solution temperature was 500 °C and the holding time was 1.5 h followed by quenching in cold water. Subsequently, the artificial aging treatment was applied at 190 °C for 6 h.

Experimental specimens were obtained from the middle part of the alloy, which is shown in Figure 2a. The welding direction was defined as the horizontal direction, while the depositing direction was defined as the vertical direction. The tensile tests were performed by the universal tensile testing machine with a tensile rate of 2 mm/min. The rod-shaped tensile specimen size is shown in Figure 2b. The Vickers micro-hardness starting at 40 mm from the bottom in units of 0.5 mm was examined along the Z-axis direction with 200 g load for 15 s.

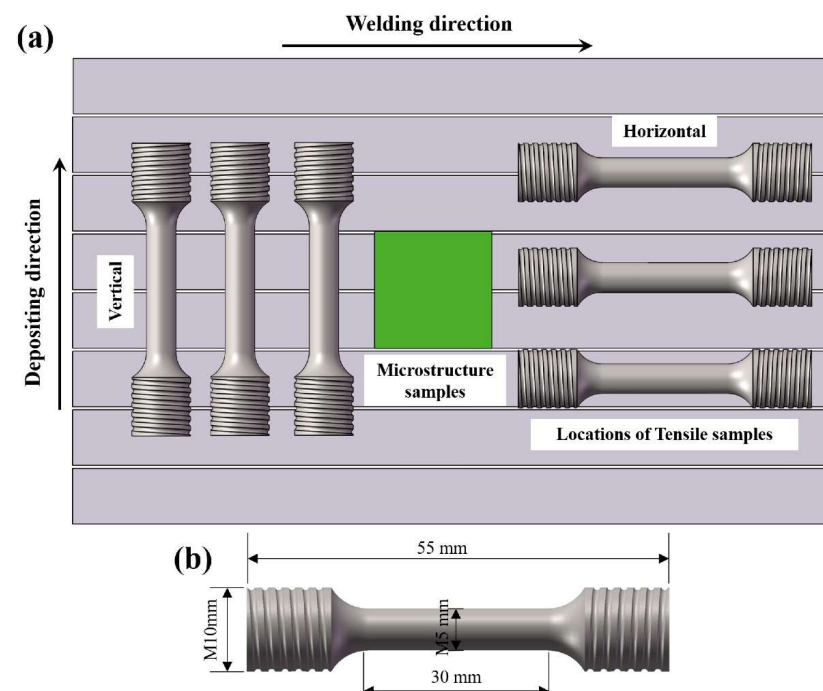


**Figure 2.** (a) The sampling positions and (b) the tensile specimen size.

The specimen sampling location for metallographic observation is shown in Figure 3. Specimens were etched by Keller solution (95 mL distilled water, 2.5 mL HNO<sub>3</sub>, 1.5 mL HCl, and 1 mL HF). The microstructure was observed by Olympus Optical microscopy (OM) (GX71, Tokyo, Japan). The phase analysis was conducted by X-ray diffractometer (XRD). The field emission scanning electron microscopy (FE-SEM), equipped with an energy dispersive spectrometer (EDS), was applied for micro-area composition detection and fractured surface morphology analysis.

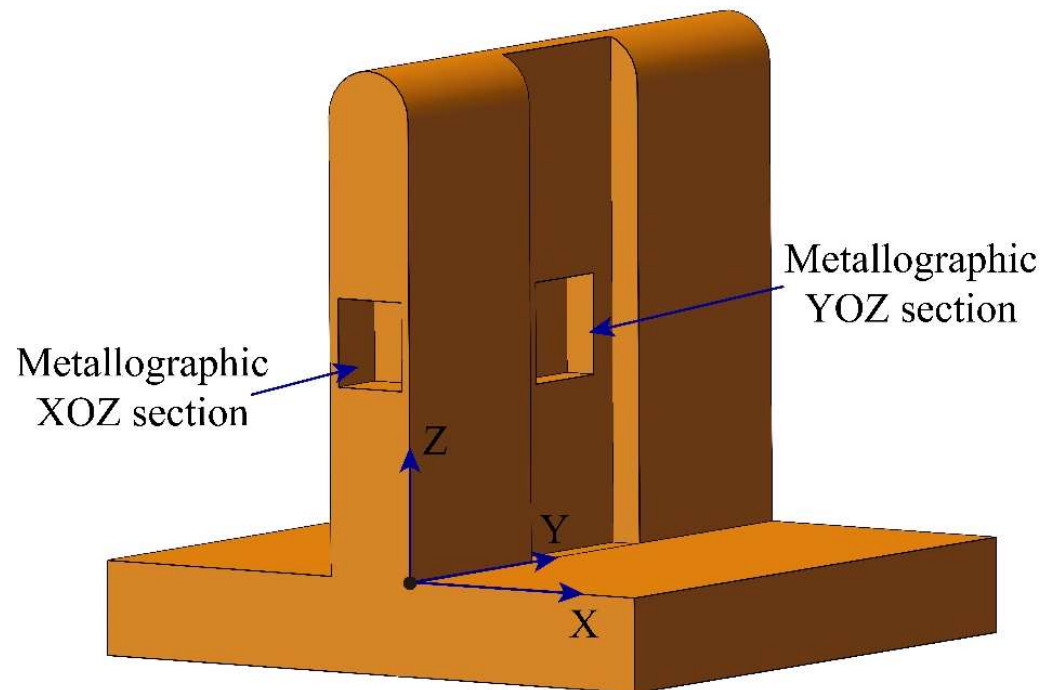


**Figure 3.** The sampling location of the specimens for metallographic observation.

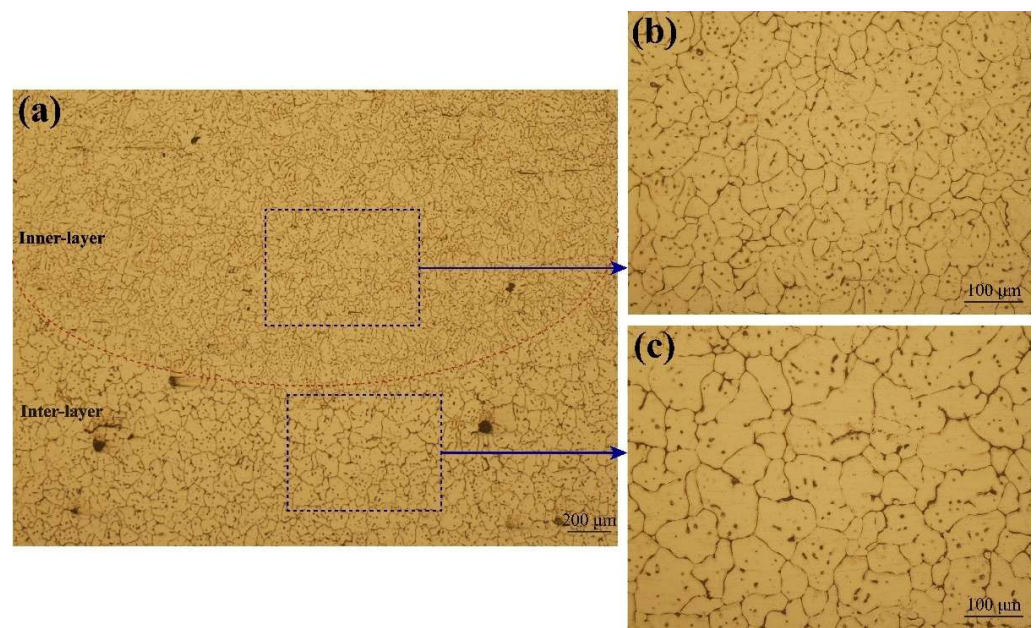
### 3. Results and Discussion

#### 3.1. Microstructure Characterization

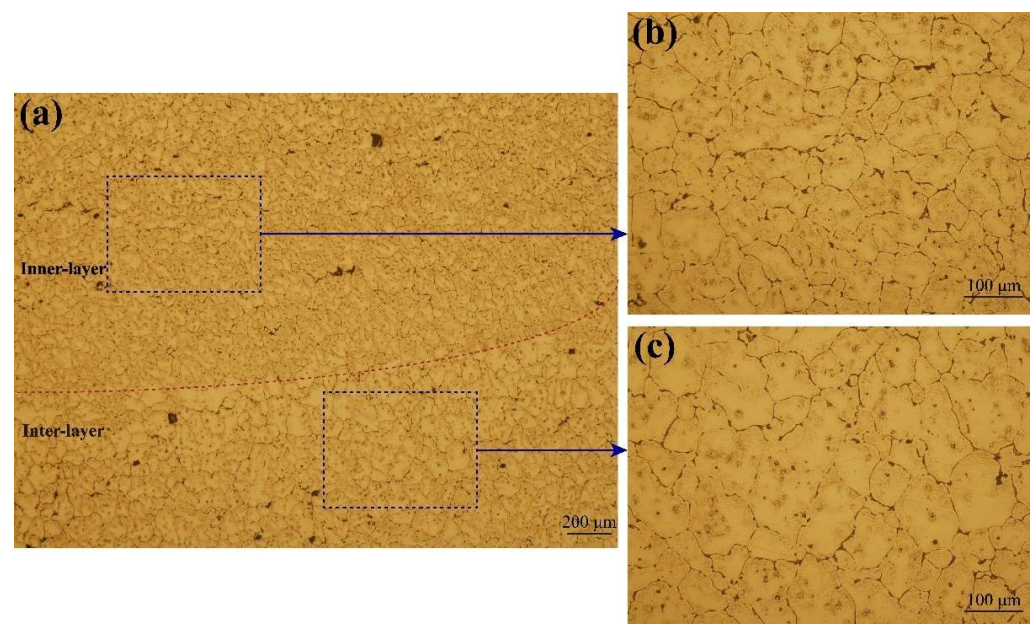
Figure 4a shows the metallographic structure of the XOZ section of the as-deposited alloy. It can be observed that the microstructure was mainly divided into the inter-layer region and inner-layer region. In the inner-layer region, the microstructure consisted of short rod-shaped columnar grains near the fusion line and coarsened equiaxed grains away from the fusion line. The average grain sizes were about 45  $\mu\text{m}$ , as shown in Figure 4b. Compared with the inner-layer microstructure, the microstructure near the fusion line in the inter-layer region was composed of coarsened equiaxed grains, which can be observed in Figure 4b. The average grain size was about 55  $\mu\text{m}$ .

Figure 5a shows the metallographic structure of the YOZ section of the as-deposited alloy. The microstructure was divided into the inter-layer region and inner-layer region by the fusion line, and the microstructure in the different regions was similar to those of the XOZ section. The average grain sizes were about 49  $\mu\text{m}$  in the inner-layer region (Figure 5b) and about 64  $\mu\text{m}$  in the inter-layer region (Figure 5c).

The microstructure of the as-deposited alloy is closely related to the temperature gradient, the cooling rate, and the number of heterogeneous nucleation nuclei [18]. In the inner-layer region, near the fusion line,  $\alpha(\text{Al})$  grains nucleated on the surface of solidified grains surface and grew inward in the form of columnar grains due to the large temperature gradient and fast cooling rate. Far from the fusion line, the heat conduction gradually decreased, the temperature gradient reduced, and the cooling rate slowed down. The  $\alpha(\text{Al})$  grains nucleated and grew up mainly through existing high melting point particles. The equiaxed grains were formed due to small differences in the temperature gradient in different directions.



**Figure 4.** (a) Microstructure of as-deposited alloy of XOZ section, (b) inner-layer region, and (c) inter-layer region.



**Figure 5.** (a) Microstructure of as-deposited alloy of YOZ section, (b) inner-layer region, and (c) inter-layer region.

ER2319 and ER5183 wires contain a certain amount of Ti and Zr elements. Ti and Zr can react with Al to form high melting point particles, such as  $\text{Al}_3\text{Ti}$  or  $\text{Al}_3\text{Zr}$ , during the welding process. The crystal structure and lattice parameters of  $\text{Al}_3\text{Ti}$  or  $\text{Al}_3\text{Zr}$  are very similar to  $\alpha(\text{Al})$ , and the lattice mismatch between them is small, which conforms to the principle of coherent interface correspondence [19,20]. Therefore, the  $\text{Al}_3\text{Ti}$  or  $\text{Al}_3\text{Zr}$  particle phase acted as heterogeneous nucleation nuclei to promote the formation of equiaxed grains. In the inner-layer region, the formed equiaxed grains hindered the epitaxial growth of columnar grains, thus forming short rod-shaped columnar grains near the fusion line, which can be observed from Figures 4a and 5a. The part of the heat-affected zone near the fusion line in the inter-layer area was affected by the arc heat, and the  $\alpha(\text{Al})$  grains had grown to a certain extent. In addition, pores and hole defects were found in the

as-deposited alloy, which was related to hydrogen absorption and incomplete inter-layer cleaning during the welding process.

Figure 6 shows the microstructure of the T6 heat-treated alloy. Compared with the as-deposited alloy, the  $\alpha(\text{Al})$  grains had significantly grown up. This is due to the high-temperature solution treatment that caused the coarsening of grains, and the average grain sizes were about  $64\ \mu\text{m}$ . In addition, more severe pores and hole defects were found in the T6 heat-treated alloy.



**Figure 6.** Microstructure of T6 heat-treated alloy.

### 3.2. The Distribution of Second Phases

According to the Al-Cu-Mg ternary phase diagram, the ternary eutectic reaction occurs at  $507\ ^\circ\text{C}$ :  $\text{L} \rightarrow \alpha(\text{Al}) + \text{S-phase} (\text{Al}_2\text{CuMg}) + \theta\text{-phase} (\text{Al}_2\text{Cu})$  during the solidification of aluminum alloy. Figure 7 shows the XRD results of as-deposited and T6 heat-treated alloys. It can be found that the as-deposited and T6 heat-treated alloys are mainly composed of  $\alpha(\text{Al})$ ,  $\theta$ -phase ( $\text{Al}_2\text{Cu}$ ), and S-phase ( $\text{Al}_2\text{CuMg}$ ). The results are consistent with the phase diagram.

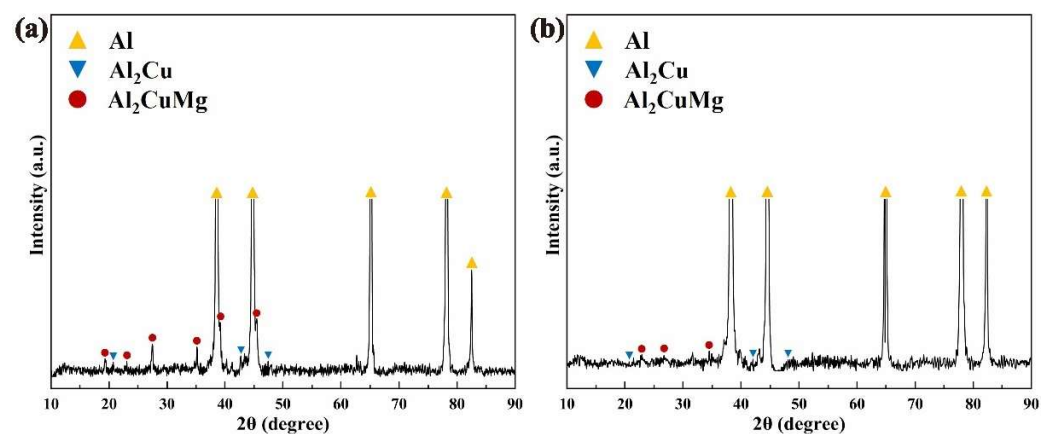


**Figure 7.** The XRD results: (a) as-deposited alloy and (b) T6 heat-treated alloy.

Figure 8a shows the backscattered electron image of the as-deposited alloy. It can be found that a large number of the second phases precipitated along the grain boundaries and within the grains, and eutectics structures were continuously distributed along the grain boundaries. Figure 8b,c show the results of the map scanning of elements, and the results of EDS point scanning are listed in Table 2. It can be found that the second phases precipitated inside the grains were mainly enriched with Cu element, which could be determined as  $\theta$ -phase ( $\text{Al}_2\text{Cu}$ ). The eutectic structures continuously distributed along the grain boundaries were mainly enriched with Cu and Mg elements, which could be determined as the binary eutectic of  $\alpha(\text{Al}) + \theta$ -phase ( $\text{Al}_2\text{Cu}$ ) or the ternary eutectic of  $\alpha(\text{Al}) + \theta$ -phase ( $\text{Al}_2\text{Cu}$ ) + S-phase ( $\text{Al}_2\text{CuMg}$ ).

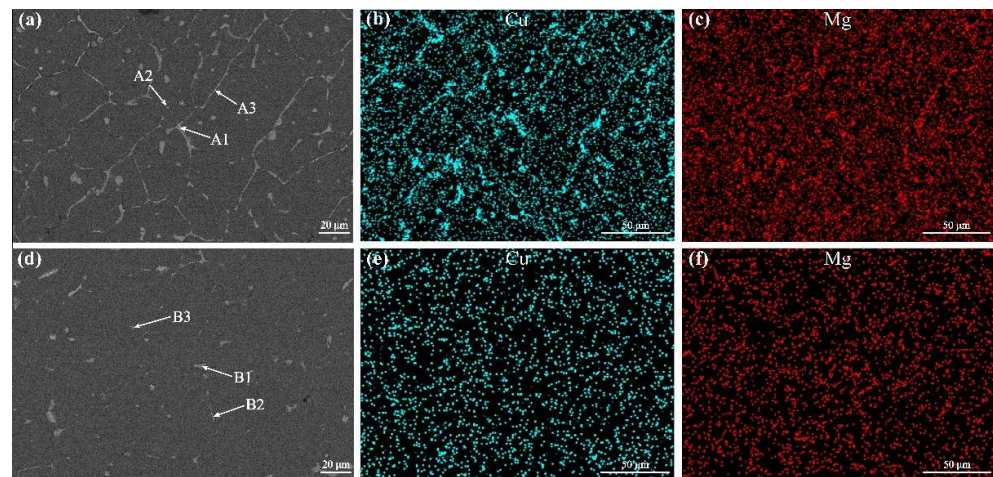


**Figure 8.** The SEM results: (a) as-deposited alloy, (b) distribution of Cu, (c) distribution of Mg, (d) T6 heat-treated alloy, (e) distribution of Cu, and (f) distribution of Mg.

**Table 2.** Chemical composition of the second phase (at%).

Positions	Al	Cu	Mg
A1	57.56	21.74	20.70
A2	78.53	11.80	9.67
A3	65.21	32.15	2.64
B1	76.81	16.18	7.01
B2	77.27	12.50	10.23
B3	80.10	15.83	4.07

After T6 heat treatment, most of the eutectic structures distributed continuously along the grain boundaries were dissolved into the  $\alpha(\text{Al})$  matrix, as shown in Figure 8d. The results of EDS point scanning and map scanning of elements demonstrate that the undissolved second phases were  $\theta$ -phase ( $\text{Al}_2\text{Cu}$ ) and S-phase ( $\text{Al}_2\text{CuMg}$ ), and the distributions of Cu and Mg elements became homogeneous, as shown in Figure 8e,f.

### 3.3. Mechanical Properties

#### 3.3.1. Micro-Hardness Tests

Figure 9 shows the micro-hardness of the middle region of as-deposited and T6 heat-treated alloys. The average micro-hardness of the as-deposited alloy was  $112 \text{ HV}_{0.2}$ , and the micro-hardness value fluctuates significantly due to the uneven distribution of Cu and Mg elements. After T6 heat treatment, the average micro-hardness was  $165 \text{ HV}_{0.2}$ , which increased by 47.3% than that of as-deposited alloy. The micro-hardness value fluctuates in the range of 158 to  $172 \text{ HV}_{0.2}$ , and the distribution was relatively uniform, which was related to the uniform distribution of Cu and Mg elements after the T6 heat treatment.

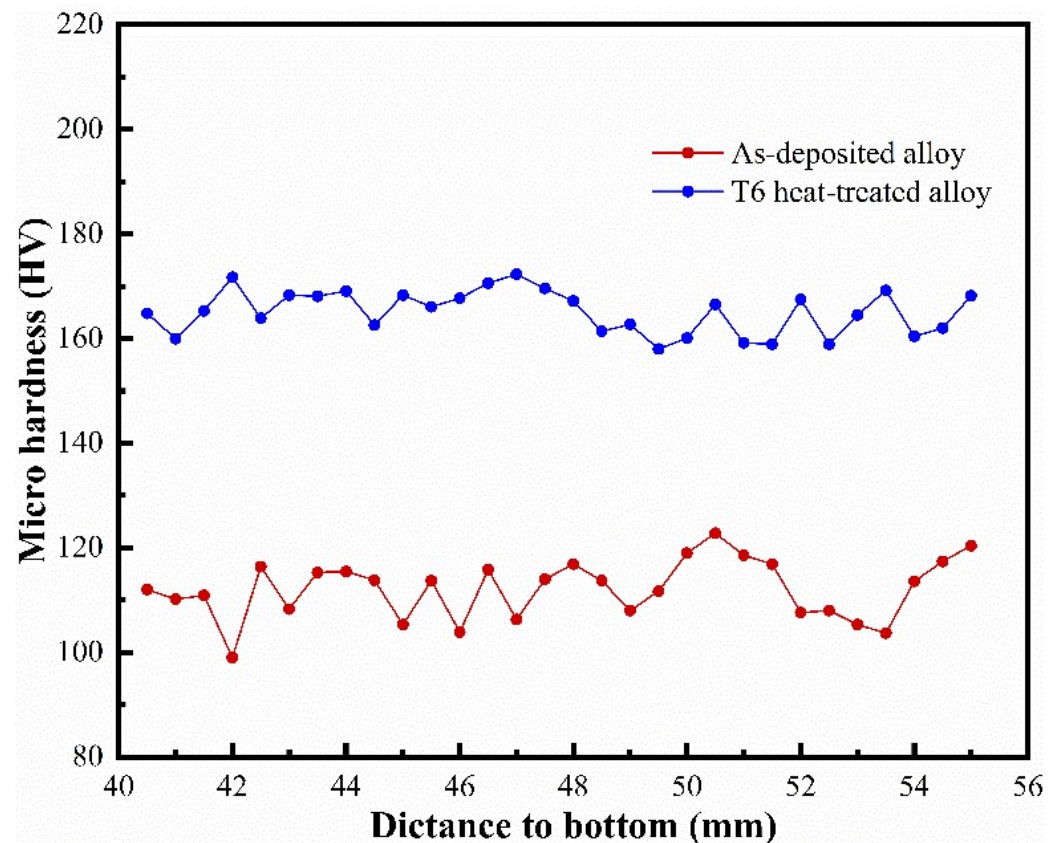


Figure 9. The micro-hardness of as-deposited and T6 heat-treated alloys.

### 3.3.2. Tensile Properties

Figure 10 shows the tensile properties of as-deposited and T6 heat-treated alloys in both horizontal and vertical directions. The UTS, YS, and elongation of the as-deposited alloy were 297 MPa, 214 MPa, and 3.6% in the horizontal direction, and 245 MPa, 198 MPa, and 2.2% in the vertical direction, respectively. After the T6 heat treatment, the UTS, YS, and elongation were 445 MPa, 387 MPa, and 2.7% in the horizontal direction, and 418 MPa, 360 MPa, and 1.8% in the vertical direction, respectively. The strengths of WAAM Al-4.7Cu-2Mg alloy after the T6 heat treatment are close to the traditional 2024-T4 plate, while the elongation is lower. It can be found that the strength and ductility of both as-deposited and T6 heat-treated alloys in the vertical direction were significantly lower than those in the horizontal direction, which was related to the existence of obvious pores and the oxide of aluminum distributed in the inter-layer region. After the T6 heat treatment, the solid solution strengthening of alloy elements and the precipitation strengthening of the secondary phases significantly improved the strengths of the alloy. However, the ductility was further reduced due to more severe pores and hole defects.

### 3.4. Fracture Analysis

Figure 11 shows the fractographic morphology of as-deposited and T6 heat-treated alloys in the horizontal direction. A large number of cleavage facets and a small number of tear ridges in the fractured surface of the as-deposited alloy can be found, and the fracture mode was mainly brittle fracture (Figure 11a). The existence of pores, hole defects, and secondary crack defects on the fractured surface reduced the strengths and ductility of WAAM alloys. After T6 heat treatment, the tear ridges on the fractured surface almost disappeared, the fracture became flatter, and the sizes of pores became significantly larger (Figure 11b). Some related research demonstrated that micro-pores will aggregate and grow during the high-temperature heat treatment of aluminum alloy, resulting in an increase in

the sizes of the pores [21,22]. More severe pores and hole defects lead to a further decline in the ductility of the alloy.

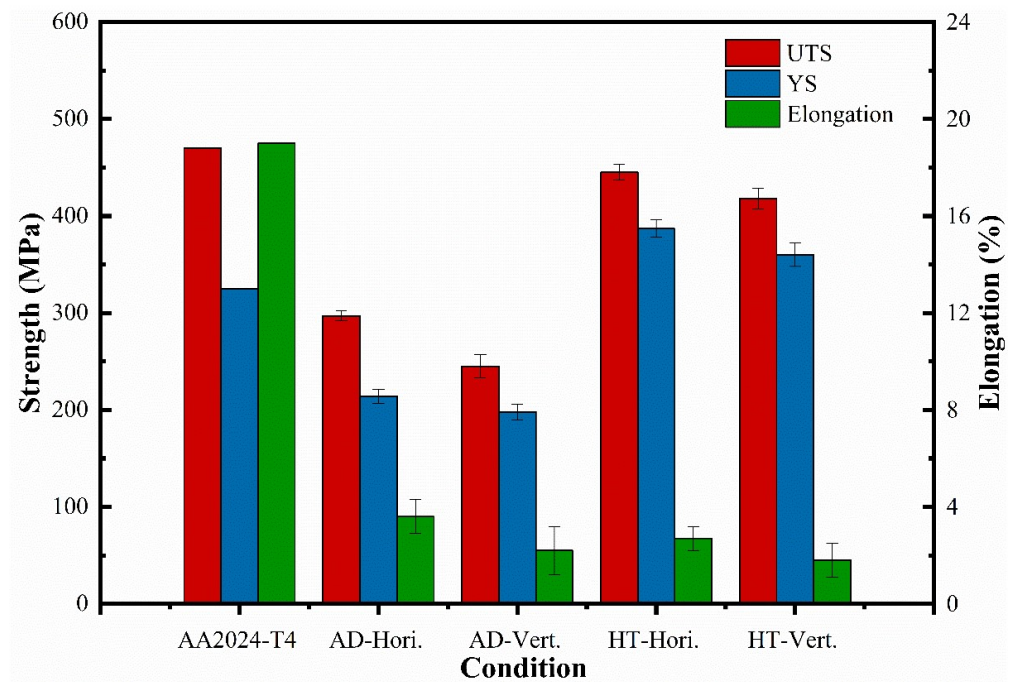


Figure 10. The tensile properties of as-deposited and T6 heat-treated alloys.

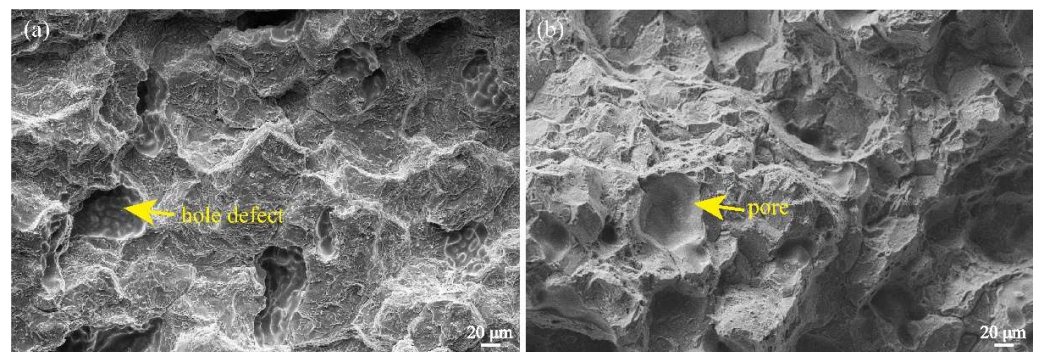


Figure 11. The fractographic morphology of alloys: (a) as-deposited alloy and (b) T6 heat-treated alloy.

#### 4. Conclusions

The Al-4.7Cu-2Mg alloy was manufactured by the double-wire CMT additive manufacturing system, and the microstructure and properties of the as-deposited and T6 heat-treated alloys were studied. The conclusions can be drawn as follows:

- (1) The microstructure of as-deposited alloy was mainly divided into the inner-layer region and the inter-layer region, and the microstructure mainly consisted of short rod-shaped columnar grains and equiaxed grains in the inner-layer region and coarsened equiaxed grains near the fusion line in the inter-layer region.
- (2) The microstructure of the as-deposited alloy was mainly composed of the second phase precipitated on the grain boundaries and the eutectic continuously distributed along the grain boundaries, and the distributions of Cu and Mg elements were inhomogeneous.
- (3) After the T6 heat treatment, most of the eutectic structure that continuously distributed along the grain boundaries dissolved into  $\alpha$ (Al) matrix and the distributions of Cu and Mg elements became homogeneous.

- (4) The tensile properties of WAAM alloys in the vertical direction were lower than that in the horizontal direction, which was related to the existence of pores and oxide of aluminum distributed in the inter-layer region. After the T6 heat treatment, the micro-hardness and strengths significantly increased. The decrease in ductility was related to the increase in the size of pores and hole defects.

**Author Contributions:** Conceptualization, S.F., X.G. (Xinpeng Guo), Y.T. and X.G. (Xuming Guo); data curation, S.F.; formal analysis, S.F., X.G. (Xinpeng Guo), Y.T. and X.G. (Xuming Guo); investigation, S.F.; methodology, S.F., X.G. (Xinpeng Guo), Y.T. and X.G. (Xuming Guo); project administration, X.G. (Xuming Guo); writing—original draft, S.F.; writing—review and editing, X.G. (Xinpeng Guo), Y.T. and X.G. (Xuming Guo). All authors have read and agreed to the published version of the manuscript.

**Funding:** This research was funded by the Major Key Technology Research Projects of Science Plan in Shenyang, grant number 20-202-1-11.

**Institutional Review Board Statement:** Not applicable.

**Informed Consent Statement:** Not applicable.

**Data Availability Statement:** Further additional data may be obtained by request to the corresponding author.

**Conflicts of Interest:** The authors declare no conflict of interest.

## References

1. Zhou, Y.H.; Lin, X.; Kang, N.; Huang, W.D.; Wang, J.; Wang, Z.N. Influence of travel speed on microstructure and mechanical properties of wire + arc additively manufactured 2219 aluminum alloy. *J. Mater. Sci. Technol.* **2020**, *37*, 143–153. [[CrossRef](#)]
2. Liu, G.C.; Xiong, J.; Tang, L. Microstructure and mechanical properties of 2219 aluminum alloy fabricated by double-electrode gas metal arc additive manufacturing. *Addit. Manuf.* **2020**, *35*, 101375. [[CrossRef](#)]
3. Sales, A.; Kotousov, A.; Yin, L. Design against Fatigue of Super Duplex Stainless Steel Structures Fabricated by Wire Arc Additive Manufacturing Process. *Metals* **2021**, *11*, 1965. [[CrossRef](#)]
4. Karayel, E.; Bozkurt, Y. Additive manufacturing method and different welding applications. *J. Mater. Res. Technol.* **2020**, *9*, 11424–11438. [[CrossRef](#)]
5. Sun, R.J.; Li, L.H.; Zhu, Y.; Guo, W.; Peng, P.; Cong, B.Q.; Sun, J.F.; Che, Z.G.; Li, B.; Guo, C.; et al. Microstructure, residual stress and tensile properties control of wire-arc additive manufactured 2319 aluminum alloy with laser shock peening. *J. Alloy. Compd.* **2018**, *747*, 255–265. [[CrossRef](#)]
6. Liu, D.; Lee, B.; Babkin, A.; Chang, Y.L. Research Progress of Arc Additive Manufacture Technology. *Materials* **2021**, *14*, 1415. [[CrossRef](#)]
7. Winterkorn, R.; Pittner, A.; Rethmeier, M. Wire Arc Additive Manufacturing with Novel Al-Mg-Si Filler Wire—Assessment of Weld Quality and Mechanical properties. *Metals* **2021**, *11*, 1243. [[CrossRef](#)]
8. Geng, R.W.; Du, J.; Wei, Z.Y.; Ma, N.S. Multiscale modelling of microstructure, micro-segregation, and local mechanical properties of Al-Cu alloys in wire and arc additive manufacturing. *Addit. Manuf.* **2020**, *36*, 101735. [[CrossRef](#)]
9. Ghaini, F.M.; Sheikhi, M.; Torkamany, M.J.; Sabbaghzadeh, J. The relation between liquation and solidification cracks in pulsed laser welding of 2024 aluminium alloy. *Mater. Sci. Eng. A* **2009**, *519*, 167–171. [[CrossRef](#)]
10. Liu, J.W.; Kou, S. Susceptibility of ternary aluminum alloys to cracking during solidification. *Acta Mater.* **2017**, *125*, 513–523. [[CrossRef](#)]
11. Fixter, J.; Gu, J.; Ding, J.; Williams, S.W.; Prangnell, P.B. Preliminary Investigation into the Suitability of 2xxx Alloys for Wire-Arc Additive Manufacturing. *Mater. Sci. Forum* **2016**, *877*, 611–616. [[CrossRef](#)]
12. Zhang, X.X.; Lv, Y.; Tan, S.H.; Dong, Z.H.; Zhou, X.R. Microstructure and corrosion behaviour of wire arc additive manufactured AA2024 alloy thin wall structure. *Corros. Sci.* **2021**, *186*, 109453. [[CrossRef](#)]
13. Gu, J.L.; Gao, M.J.; Yang, S.L.; Bai, J. Microstructure, defects, and mechanical properties of wire + arc additively manufactured Al-Cu4.3-Mg1.5 alloy. *Mater. Des.* **2020**, *186*, 108357. [[CrossRef](#)]
14. Qi, Z.W.; Cong, B.Q.; Qi, B.J.; Sun, H.Y.; Zhao, G.; Ding, J.L. Microstructure and mechanical properties of double-wire + arc additively manufactured Al-Cu-Mg alloys. *J. Mater. Process. Technol.* **2018**, *255*, 347–353. [[CrossRef](#)]
15. Gu, J.L.; Bai, J.; Ding, J.L.; Williams, S.; Wang, L.M.; Liu, K. Design and cracking susceptibility of additively manufactured Al-Cu-Mg alloys with tandem wires and pulsed arc. *J. Mater. Process. Technol.* **2018**, *262*, 210–220. [[CrossRef](#)]
16. Fang, X.W.; Zhang, L.J.; Chen, G.P.; Huang, K.; Xue, F.; Wang, L.; Zhao, J.Y.; Lu, B.H. Microstructure evolution of wire-arc additively manufactured 2319 aluminum alloy with interlayer hammering. *Mater. Sci. Eng. A* **2021**, *800*, 140168. [[CrossRef](#)]
17. Fang, X.W.; Zhang, L.J.; Yang, J.N.; Bai, H.; Zhao, L.; Huang, K.; Lu, B.H. Effect of characteristic substrate parameters on the deposition geometry of CMT additive manufactured Al-6.3%Cu alloy. *Appl. Therm. Eng.* **2019**, *162*, 114302. [[CrossRef](#)]

18. Wang, Z.N.; Lin, X.; Wang, L.L.; Cao, Y.; Zhou, Y.H.; Huang, W.D. Microstructure evolution and mechanical properties of the wire + arc additive manufacturing Al-Cu alloy. *Addit. Manuf.* **2021**, *47*, 102298. [[CrossRef](#)]
19. Zheng, Q.; Yang, C.; Wang, S.; Yu, A.; Chen, H.; He, Y. Effect of compound inoculants Ti and Zr on as-cast microstructure and mechanical properties of Al-Cu alloy. *Mater. Res. Innov.* **2014**, *18*, 59–63. [[CrossRef](#)]
20. Atamanenko, T.V.; Eskin, D.G.; Sluiter, M.; Katgerman, L. On the mechanism of grain refinement in Al-Zr-Ti alloys. *J. Alloy. Compd.* **2011**, *509*, 57–60. [[CrossRef](#)]
21. Gu, J.L.; Ding, J.L.; Williams, S.W.; Gu, H.M.; Ma, P.H.; Zhai, Y.C. The effect of inter-layer cold working and post-deposition heat treatment on porosity in additively manufactured aluminum alloys. *J. Mater. Process. Technol.* **2016**, *230*, 26–34. [[CrossRef](#)]
22. Toda, H.; Hidaka, T.; Kobayashi, M.; Uesugi, K.; Takeuchi, A.; Horikawa, K. Growth behavior of hydrogen micropores in aluminum alloys during high-temperature exposure. *Acta Mater.* **2009**, *57*, 2277–2290. [[CrossRef](#)]